Modelling the Positional and Orientation Sensitivity of Proximity Sensors for Industrial IoT

Richard McWilliam and Alan Purvis
School of Engineering and Computing Sciences
Durham University
Durham, DH1 3LE, United Kingdom
r.p.mcwilliam@durham.ac.uk, alan.purvis@durham.ac.uk

Samir Khan
School of Mechanical, Automotive and Aerospace Engineering
Coventry University
Coventry, CV1 5FB, United Kingdom
ac0160@coventry.ac.uk

***Abstract*—This paper presents an analysis of robust proximity sensor interfaces for Industrial Internet of Things applications. A Model is presented with the aim of maximizing the range and freedom of orientation of passive sensing and communications devices in comparison to traditional source-sensor technologies. A matrix transformation approach is used to model the quality of mutual coupling between triaxial source and sensor coil arrangements for arbitrary relative position and angular rotation. Particular attention is paid to the recombination of triaxial sensor outputs and optimal rotation for maximal coverage given a specified coupling threshold. The model is useful for determining practical source-sensor configurations that achieve optimal coverage when the sensor position and rotation is restricted by the industrial application.**

Keywords–Internet of things; Industrial sensing; Radio frequency identification; Inductive coupling

I. Introduction

Robust sensing devices for Industrial Internet of Things (I-IoT) is a key enabling technology for future smart wireless sensor networks driven by the need for pervasive, fine-grained embedded sensing, communications and asset management capabilities [1], [2]. Passive and orientation-free sensing is of significant interest for supporting confined and harsh-environment industrial systems prognostic, asset management and efficiency monitoring applications where fully active sensing is otherwise difficult or impossible using current technologies constrained by cost, weight or volume limitations [3]. At the same time, established RFID sensors and electronics tend to be limited to highly constrained transponder orientations that, while tolerable among e-commerce applications, imposes a severe limitation for orientation sensitive I-IoT environments.

Proximity sensor networks are beginning address the needs of I-IoT and will become integrated within the 5G ecosystem [4]. However, a number of opportunities exist to extend the reach of I-IoT right to the edge of the operational environment of cyber physical systems (CPS) by incorporating more compact and robust passive sensing technologies for example, within security networks [5]. The potential benefits are significant: high quality information generated by monitoring, diagnosis and tracking sensory networks close to the cyber-physical edge of hardware environment boundaries. However, its integration within I-IoT is less clear due to the practical limitations of placement and orientation sensitivity and power efficiency. As a result, many I-IoT data collection platforms still favour hard-wired integrated sensor networks [6].

In this paper, a free-space orientation model for power and communication is proposed based on triaxial source and triaxial sensor coils. Such arrangements are becoming feasible through advances in 3D additive manufacturing technologies capable of integrating conductive tracks and integrated circuits within the mechanical assembly. Several radial coil source/sensor combinations are studied in terms of their impact on sensor coverage defined over the shell of a unit sphere.

II. Proximity Sensing and Industrial IoT

Although there are similarities between I-IoT and the comparatively mature IoT infrastructures that exist in e-commerce ticketing and product supply chains [7], there are fundamental differences with respect to the expected robustness and availability of industrial hardware platforms that must be dependable within confined and harsh operational environments. It is well known that the inherently localized nature of near-field contactless sensing offers an inherent security zone for sensitive assets as well as orientation detection [8]. A core challenge is the energy efficiency of IoT sensor networks that directly affects the Quality of Service (QoS) in industrial applications [1]. Energy efficiency may optimized through network protocols [9], RF chip design [10] and coupling efficiency. For proximity sensing, coupling efficiency is affected by both orientation and the surrounding environment [11].

Proximity I-IoT sensing hardware extends far beyond existing e-commerce domains found in IoT and there are many opportunities for innovation in this sector. For example, sensor networks for jet engine test beds must survive high temperature and vibration conditions whilst providing high data bandwidth telemetry during test.

978-1-5090-0888-9/16 $31.00 © 2016 IEEE
DOI 10.1109/UKSim.2016.11

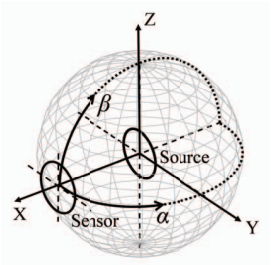

Figure 1. Geometry of single source and single sensor coils when oriented in the X-direction and restricted to the shell of a unit sphere. Sensor position is described on unit sphere by angular variables (α, β).

Traditional proximity sensors utilise a single source and sensor coil arrangement, whereby power and communications are supported by co-planar inductive coupling. This arrangement is depicted in Fig. 1 where the sensor position lies on the shell of a sphere of radius r and the received power to source-sensor separation, d, decays according to d^{-6}. While this arrangement has become the standard interface for proximity sensing [12], coupling efficiency is highly dependent upon orientation.

Non-planar coil arrangements have been proposed to reduce orientation sensitivity by fabricating embedded orthogonal tracks within the sensor volume [13], [14]. However, it is still difficult to predict their performance within confined packaging and dampening effects caused by the presence of foreign materials further compounding the need for careful pre-planning and prediction of the expected coupling geometry. For this reason, the coupling efficiency of simpler triaxial coil arrangements is considered here.

III. Physical Couping Model

Proximity coupling is modelled as a inductive source-sensor arrangement as depicted in Fig. 1. For the case shown, the transmitting and receiving coils are nominally arranged such their respective magnetic moments are aligned i.e., the coils are co-planar oriented along the x-axis. It has been assumed that the coil radius a is considerably smaller than the coil separation r (or more strictly $a^2 < r^2$). With reference to Fig. 2, mutual interaction occurs between the magnetic field components of each coil, which are described according to the radial and tangential field equations:

$$H_r = \frac{M}{r^3}\cos\beta \qquad H_t = \frac{M}{2r^2}\sin\beta \qquad M = \frac{a^2 IN}{2}, \quad (1)$$

where H_r and H_t are the radial and tangential field components respectively, β is the angle of elevation between the magnetic moment vector and position of observation, I is the magnitude of alternating current passing through each coil and N is the number of coil turns.

A. Orthogonal and Co-planar Coil Arrangements

Considering initially a single source and sensor coil pair, three orthogonal arrangements are considered as illustrated in Fig. 3(a-c). The source coil assumes a fixed position oriented along the x-axis and is referred to as an X-source coil. Adopting similar nomenclature for the sensor coil, each of the X, Y- and Z-sensor coil orientations can be seen. Clearly mutual coupling exists only for the case of X-sensor (radial coupling) while other combinations experience zero coupling due to orthogonality. Thus, each of the co-planar and orthogonal cases can be represented by the coupling equation:

$$\boldsymbol{S_{out}} = \frac{M}{r^3}\begin{bmatrix} 1 & 0 & 0 \\ 0 & -0.5 & 0 \\ 0 & 0 & -0.5 \end{bmatrix}\boldsymbol{S_{src}} = \frac{M}{r^3}\boldsymbol{O}\boldsymbol{S_{src}}, \quad (2)$$

where $\boldsymbol{O}$ is a constant matrix termed the orientation matrix and the input and output coil signals are written in vector form:

$$\boldsymbol{S_{src}} = \begin{bmatrix} S_{srcx} \\ S_{srcy} \\ S_{srcz} \end{bmatrix}, \boldsymbol{S_{out}} = \begin{bmatrix} S_{outx} \\ S_{outy} \\ S_{outz} \end{bmatrix}. \quad (3)$$

Referring again to Fig. 1, (2) describes the combined coupling between three orthogonal source coils placed at the origin of a unit sphere ($r = 1$) and three orthogonal sensor coils placed on the x-axis at $x = 1$. Since $\boldsymbol{O}$ is a diagonal matrix, orthogonal source/sensor pairs contribute zero coupling, while co-planar pairs contribute radial or tangential field coupling.

B. Influence of Sensor Position and Orientation

The matrix representation (2) permits the inclusion of additional source-sensor contributions that arise when the sensor position and orientation is no longer confined to the x-axis. Depending on the application requirements, the sensor coil ensemble may be expected to change position or orientation relative to the source ensemble, in which case the expected variations of coupling must be known. Sensor position is accounted for by azimuthal (α) and elevation (β) angles (see Fig. 1) while sensor orientation is described according to azimuthal (ψ) elevation (θ) and roll (ϕ) rotations (see Fig. 4). Single, dual- or tri-source and sensor coils ensembles are handled by assigning or evaluating the respective elements of vectors (3). If the co-planar arrangements of Fig. 3 are imposed then only azimuth

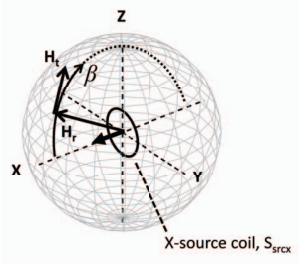

Figure 2. Basic coordinate system showing X-oriented source coil.

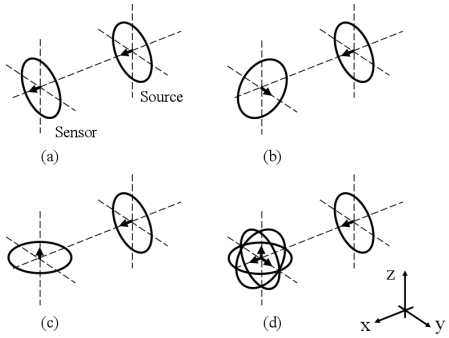

Figure 3. Example X-source coil and various sensor coil orientations. (a) X-sensor. (b) Y-sensor. (c) Z-sensor. (d) Tri-sensor.

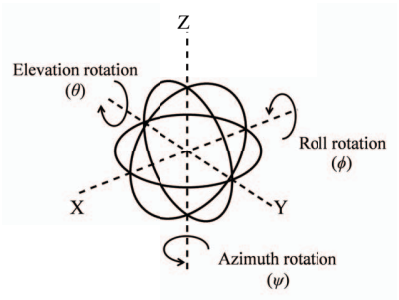

Figure 4. Rotation geometry for orthogonal sensor arrangements.

and elevation rotation need be considered while roll rotation must be included when dual- or triaxial coils are used.

Given the above description, the problem may then be generalized by applying the method of Raab *et al.* [15] for positional and orientation transformation, wherein a sequence of positional and rotational transformations

$$\begin{aligned}
&\text{(Azimuth position)} && \boldsymbol{T_\alpha} = \begin{bmatrix} \cos\alpha & \sin\alpha & 0 \\ -\sin\alpha & \cos\alpha & 0 \\ 0 & 0 & 1 \end{bmatrix} \\
&\text{(Elevation position)} && \boldsymbol{T_\beta} = \begin{bmatrix} \cos\beta & 0 & -\sin\beta \\ 0 & 1 & 0 \\ \sin\beta & 0 & \cos\beta \end{bmatrix} \\
&\text{(Azimuth rotation)} && \boldsymbol{T_\psi} = \begin{bmatrix} \cos\psi & \sin\psi & 0 \\ -\sin\psi & \cos\psi & 0 \\ 0 & 0 & 1 \end{bmatrix} \\
&\text{(Elevation rotation)} && \boldsymbol{T_\theta} = \begin{bmatrix} \cos\theta & 0 & -\sin\theta \\ 0 & 1 & 0 \\ \sin\theta & 0 & \cos\theta \end{bmatrix} \\
&\text{(Roll rotation)} && \boldsymbol{T_\phi} = \begin{bmatrix} 1 & 0 & 0 \\ 0 & \cos\phi & \sin\phi \\ 0 & -\sin\phi & \cos\phi \end{bmatrix}
\end{aligned} \tag{4}$$

are applied to the orientation matrix $\boldsymbol{O}$. The aggregate sensor output is then determined by the expression:

$$\boldsymbol{S_{out}} = \frac{M}{r^3} \boldsymbol{f_o}(\psi,\theta,\phi) \boldsymbol{f_p}(\alpha,\beta) \boldsymbol{S_{src}}, \tag{5}$$

where $\boldsymbol{f_p} = \boldsymbol{T_{-\alpha}} \boldsymbol{T_{-\beta}} \boldsymbol{O} \boldsymbol{T_\beta} \boldsymbol{T_\alpha}$, $\boldsymbol{f_o} = \boldsymbol{T_\phi} \boldsymbol{T_\theta} \boldsymbol{T_\psi}$ account for sensor position and orientation respectively. The application of transformation operation successively alters the orientation matrix to account for sensor position and orientation, after which a final transformation of the form (2) yields $\boldsymbol{S_{out}}$. Azimuthal and elevation position are accounted for by a two-step transformation process, in which forward/reverse transformations of an equivalent source coil aligned to the sensor coil takes places, while the polarities of the α, β indicies determine the direction of transformation [15]. Except for the simple orthogonal arrangements considered in (2), the transformation matrices create new contributions within the non-diagonal elements of $\boldsymbol{O}$.

From the above model, the quality of mutual coupling in each of the x-,y- and z-directions may be defined by the individual ratios S_{outx}/S_{srcx} etc., or else directly by the values elements of $\boldsymbol{S_{out}}$ for the case of unity valued source inputs.

IV. Simulation Results and Analysis

Graphical representations of coupling quality were generated by a Matlab script that evaluates (5) over n discrete sensor positions $\alpha = [-\pi \ldots 2\pi/(n-1) \ldots \pi]$ and $\beta = [-\pi/2 \ldots \pi/(n-1) \ldots \pi/2]$. Normalized electrical and separation conditions have been assumed (i.e., $M = r = 1$).

A. Co-planar coils

To confirm the basic model, the simplest case of an X-source and X-sensor coil (see Fig. 3(a)) was evaluated using $n = 200$. The resulting variations of coupling for a single X-sensor coil is presented in Fig. 5(a) as a two-dimensional surface representation of coupling quality rendered on a discrete grid comprising 200x200 azimuth and elevation positions.Basic statistical properties summarized in Table I. Regions of weak and null coupling appear in the distribution, severely limiting the useful range of acceptable sensor positions. Adopting instead a single Y-sensor coil, similar map of $\boldsymbol{S_{outy}}$ is generated as illustrated in Fig. 5(b). In this case peak, coupling reaches a lower normalized value of 0.75 in comparison to the X-sensor case due to the lack of radial field contributions but with a more uniform spread of positive and negative values as indicated by the zero mean value. The result for a single Z-sensor coil (not shown) is similar to that of the Y-sensor coil.

An alternative visualization of the above results is presented in Fig. 6 wherein the equivalent maps have been superimposed over a spherical shell. The localization of field null regions can immediately be identified as taking the form of circular/elliptical annuli. Such regions exist for all single sensor coil arrangements.

B. Triaxial coil and sensor

The results presented above confirm that singular sensor coil arrangements do not achieve elimination of field coupling nulls. Hence, a single X-source and triaxial coil sensor

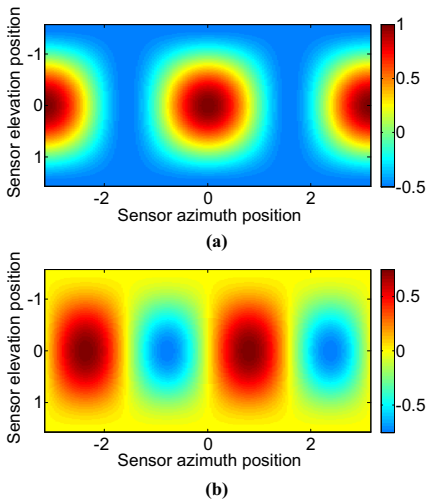

Figure 5. Examples of two-dimensional coupling maps. (a) X-sensor (b) Y-sensor (units in radians).

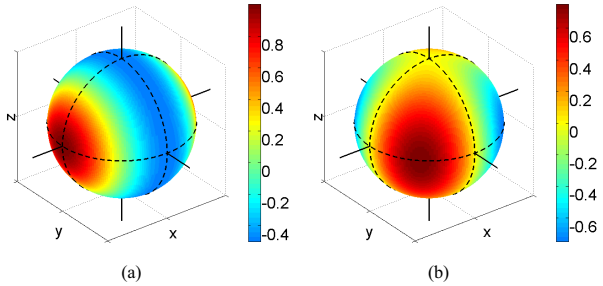

Figure 6. 3D visual maps created by X-source and X/Y-sensor coil coupling. (a) X-sensor coupling. (b) Y-sensor coupling.

arrangement was adopted. There are a number of possible sensor recombination operations f_c, noting further that phase sensitive recombination is limited to the received polarities $[0, \pi]$:

1) Direct summation: The simplest recombination approach involves a direct vector summation of each coil output, $S_{out\_comb} = S_{outx} + S_{outy} + S_{outz}$.

2) Rectify-sumation: Rectify-summation involves the simplest practical operation of combining the outputs produced by idealized diodes connected to each sensor output, $S_{out\_comb} = |S_{outx}| + |S_{outy}| + |S_{outz}|$.

3) Best coil selection: Best coil selection involves detecting and selecting the strongest (absolute) coupled voltage from any single coil for a given position, $S_{out\_comb} = max\left(|S_{outx}|, |S_{outy}|, |S_{outz}|\right)$.

4) RMS: The RMS approach applies the expression $S_{out\_comb} = \left[1/3\left(S_{outx}^2 + S_{outy}^2 + S_{outz}^2\right)\right]^{1/2}$, which is proportional to the average coupled power from the tri-sensor. Visual results are presented in Fig. 7 along with key evaluation metrics in Table I. For the direct summation

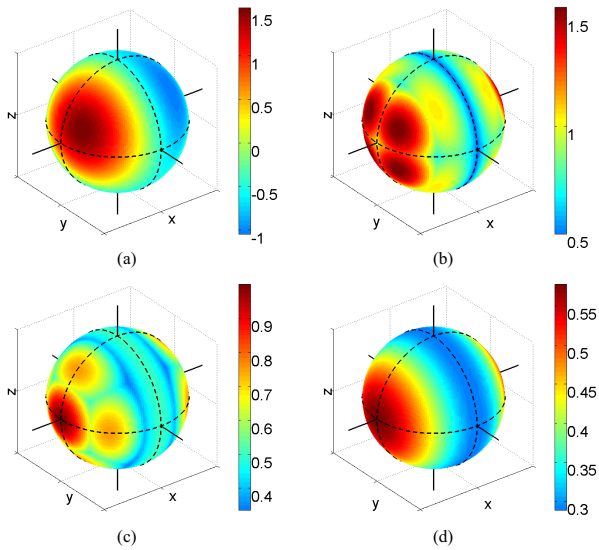

Figure 7. Tri-sensor output produced by various recombination methods and for a single X-source coil. (a) Direct summation method. (b) Rectify-summation method. (c) Best coil output selection (based on absolute value). (d) RMS.

method, field nulls persist around annular regions (Fig. 7a) while the normalized sensor output lies between +1.57 and -1.05—extended in comparison to the single X-source coil due to the additional Y- and Z-sensor contributions—but accompanied by highly localized regions of strong coupling. This view is supported by low arithmetic mean and high standard deviation values.

Direct summation results in regions of null coupling due to the preservation of phase inversions within the linear summation operation, a problem that is overcome by adopting one of the alternative recombination methods. Comparative results are presented in Fig. 7(b-d) and Table I for each approach. In addition, a direct comparison of the variations in coupling extracted along the equatorial line of the unit sphere is plotted in Fig. 8, where the smoothing effect of the RMS approach is apparent. The best overall performance is seen for the best coil and rectify-sum methods, though these approach assume that the I-IoT application is tolerant to the more confined regions of strong coupling and rapid variations therein.

C. Application-Specific Constraints

Given the above characterisation and the chosen arrangement of X-source and tri-sensor coils, application-specific considerations may be investigated by applying a series of constraints on the expected coverage C threshold coupling quality t and position/orientation freedom of the sensor. In this context, C is calculated as the percentage area lying on the unit sphere over which t is exceeded.

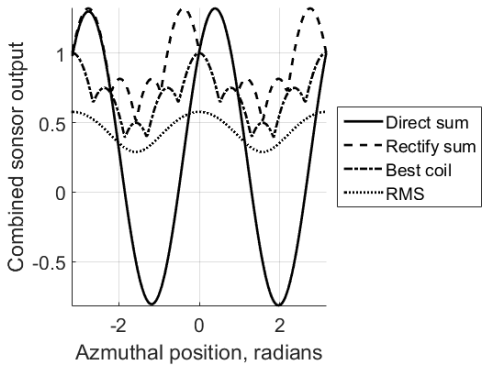

Figure 8. Plots of coupled signal produced by tri-sensor coil and X-source coil plotted along the equatorial line of the unit sphere ($-\pi \leq \alpha \leq \pi, \beta = 0$).

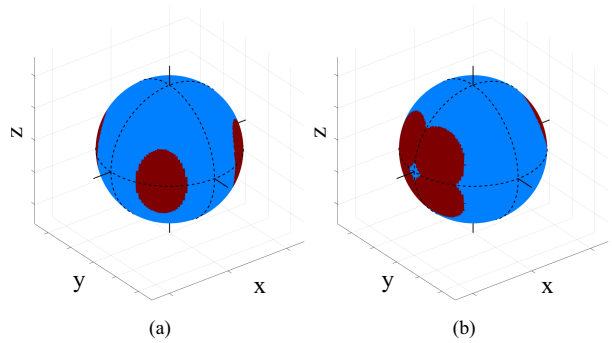

Figure 9. Threshold-delimited coupling maps for (a) single Y-sensor and (b) tri-sensor with rectify-summation method. Red shaded regions indicate where the output exceeds 75% of the maximum output; blue shaded regions indicate regions where coupling is insufficient.

TABLE I
STATISTICAL PROPERTIES OF SINGLE OUTPUT COIL AND TRI-COIL RECOMBINATIONS METHODS ACROSS ALL DISCRETE POSITIONS OF A ZERO-ORIENTATION TRI-COIL SENSOR.

	Max	Min	Mean	SD[a]	C[b] (t=0.75)
Single x-sensor	1.00	-0.50	-0.13	0.42	5.75%
Single y-sensor	0.75	-0.75	≈ 0	0.32	12.15%
Single z-sensor	0.75	-0.75	≈ 0	0.38	17.08%
Direct-sum	1.55	-1.05	-0.13	0.65	6.10%
Rectify-sum	1.55	0.50	0.93	0.28	21.26%
Best coil	1.00	0.34	0.55	0.13	5.77%
RMS	0.58	0.29	0.37	0.09	25.00%

[a]SD=standard deviation.
[b]C=Coverage for specified threshold t.

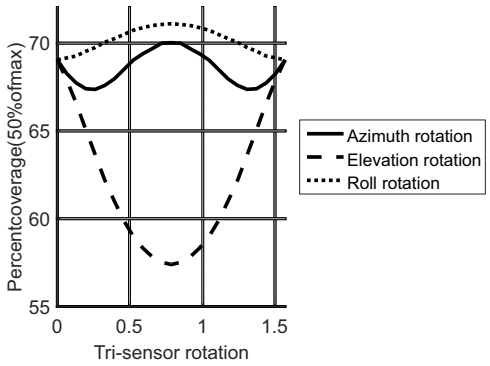

Figure 11. Calculated coverage distributions versus tri-sensor rotation with single X-source coil. For the cases shown, rectify sum sensor recombination is used and a threshold $t = 0.5$ was specified.

1) Threshold-delimited coverage: The single and triaxial coil arrangements may be further characterized by computing C over the discretized $n \times n$ grid of sensor positions. Choosing $t = 0.75$, the cases of a single Y-sensor and triaxial coil sensor utilizing the rectify-summation method are visualized in Fig. 9, where the maps have been divided into regions remarking the acceptable/unacceptable sensor positions. Referring again to Table I, the corresponding coverage values show that the rectify-summation method achieves a coverage 1.75x higher than the single Y-sensor. Further comparisons may be drawn from inspection of Table I and evaluation of (5) for different t.

2) Restricted sensor position: Choosing once more the rectify-summation method and applying a nominal sensor rotation of $\pi/4$ for each of the rotation directions in turn, the resulting coupling variations are shown visually in Fig. 10. Further insight into the sensitivity to sensor rotation is gained by aggregating the coverage results across a range of sensor positions and orientations. An example of this is presented in Fig. 11, for which rotations were applied over the range $[0, \pi]$ and $t = 0.5$. For this case, appreciable sensitivity to sensor rotation is observable and maxima for $\psi = \theta = \pi/4$, but a corresponding minimum for the case of roll rotation.

3) Non-equal sensor geometry: Another consideration is the relative area available for each of the triaxial sensor coils, which may be non-identical. A relatively subtle instance of this is visualized in Fig. 12a, in which the area of a Z-oriented sensor has been reduced to 1/3 relative to that of the X- and Y-sensors by scaling S_{outz}. In this case the regions of maximal coupling about the X-axis become more widely spread (cf. Fig. 7(b)) with potential benefits for some applications. Overall coverage is however reduced by 27% in comparison to the equal-area triaxial sensor. As the sensor orientation is altered the resulting coverage may be evaluated, an example of which is seen in Fig. 12b.

V. CONCLUSION

The presented position and orientation coupling model permits detailed investigation of arbitrary single, dual- and tri-axial coil source/sensor configurations including recom-

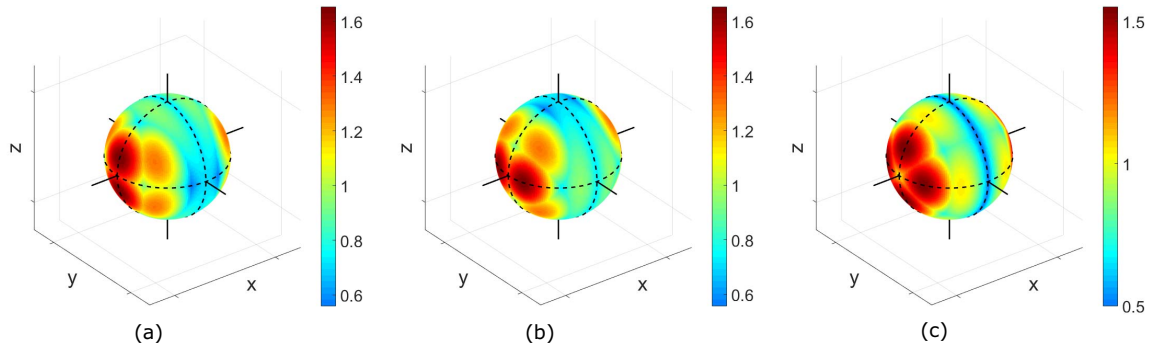

Figure 10. Effect of rotation of triaxial coil. (a) Azimuth rotation by $\pi/4$. (b) Elevation rotation by $\pi/4$. (c) Roll rotation by $\pi/4$.

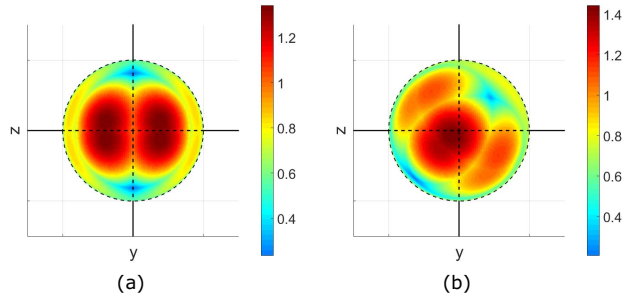

Figure 12. Example of X-source and triaxial coil coupling where the Z-oriented coil is 33% smaller than the X- and Y-oriented coils and using the rectify-summation method. (a) Zero-orientation. (b) Sensor rotated to $\psi = \pi/8, \phi = \pi/4, \theta = -\pi/8$.

bination methods, from which it is observed that the rectify-summation method provides a favourable combination of ease of implementation and high coverage. The inclusion of tri-sensor coils brings significant improvements to the robustness of source-sensor coupling—a necessary property for delivering high quality, robust I-IoT sensing. The model can be further extended to include close proximity coupling ($a \approx r$), though the inclusion of all near-field effects is a complex task.

Acknowledgment

This work was supported by the UK EPSRC Centre for Innovative Manufacturing in Through-life Engineering Services (EP/I033246/1).

References

[1] L. D. Xu, W. He, and S. Li, "Internet of Things in Industries: A Survey," *IEEE Transactions on Industrial Informatics*, vol. 10, no. 4, pp. 2233–2243, Nov. 2014.

[2] J. M. Tien, "Internet of connected ServGoods: Considerations, consequences and concerns," *Journal of Systems Science and Systems Engineering*, vol. 24, no. 2, pp. 130–167, May 2015.

[3] L. Atzori, A. Iera, and G. Morabito, "The Internet of Things: A survey," *Computer Networks*, vol. 54, no. 15, pp. 2787–2805, Oct. 2010.

[4] Z. Ma, Z. Zhang, Z. Ding, P. Fan, and H. Li, "Key techniques for 5g wireless communications: network architecture, physical layer, and MAC layer perspectives," *Science China Information Sciences*, vol. 58, no. 4, pp. 1–20, Feb. 2015.

[5] T. Vollmer, M. Manic, and O. Linda, "Autonomic Intelligent Cyber-Sensor to Support Industrial Control Network Awareness," *IEEE Transactions on Industrial Informatics*, vol. 10, no. 2, pp. 1647–1658, May 2014.

[6] Z. Hajduk, B. Trybus, and J. Sadolewski, "Architecture of FPGA Embedded Multiprocessor Programmable Controller," *IEEE Transactions on Industrial Electronics*, vol. 62, no. 5, pp. 2952–2961, May 2015.

[7] K. Finkenzeller, *RFID Handbook: Fundamentals and Applications in Contactless Smart Cards, Radio Frequency Identification and Near-field Communication*, 3rd ed. Chichester, West Sussex ; Hoboken, NJ: Wiley-Blackwell, Jun. 2010.

[8] G. Gupta, B. P. Singh, A. Bal, D. Kedia, and A. R. Harish, "Orientation Detection Using Passive UHF RFID Technology [Education Column]," *IEEE Antennas and Propagation Magazine*, vol. 56, no. 6, pp. 221–237, Dec. 2014.

[9] B. Martinez, M. Monton, I. Vilajosana, and J. Prades, "The Power of Models: Modeling Power Consumption for IoT Devices," *IEEE Sensors Journal*, vol. 15, no. 10, pp. 5777–5789, Oct. 2015.

[10] P. Wei, W. Che, Z. Bi, C. Wei, Y. Na, L. Qiang, and M. Hao, "High-Efficiency Differential RF Front-End for a Gen2 RFID Tag," *IEEE Transactions on Circuits and Systems II: Express Briefs*, vol. 58, no. 4, pp. 189–194, Apr. 2011.

[11] X. Qing and Z. N. Chen, "Proximity Effects of Metallic Environments on High Frequency RFID Reader Antenna: Study and Applications," *IEEE Transactions on Antennas and Propagation*, vol. 55, no. 11, pp. 3105–3111, Nov. 2007.

[12] X. Mou and H. Sun, "Wireless Power Transfer: Survey and Roadmap," in *Vehicular Technology Conference (VTC Spring), 2015 IEEE 81st*, May 2015, pp. 1–5.

[13] S. Sasaki, T. Seki, K. Imanaka, M. Kimata, T. Toriyama, T. Miyano, and S. Sugiyama, "Batteryless-Wireless MEMS Sensor System with a 3d Loop Antenna," in *2007 IEEE Sensors*, Oct. 2007, pp. 252–255.

[14] C. Kruesi, R. Vyas, and M. Tentzeris, "Design and Development of a Novel 3-D Cubic Antenna for Wireless Sensor Networks (WSNs) and RFID Applications," *IEEE Transactions on Antennas and Propagation*, vol. 57, no. 10, pp. 3293–3299, Oct. 2009.

[15] F. Raab, E. Blood, T. Steiner, and H. Jones, "Magnetic Position and Orientation Tracking System," *IEEE Transactions on Aerospace and Electronic Systems*, vol. AES-15, no. 5, pp. 709–718, Sep. 1979.